RSC Advances

PAPER

View Article Online
View Journal | View Issue

Cite this: *RSC Adv.*, 2021, **11**, 24508

A defect-rich ultrathin MoS_2/rGO nanosheet electrocatalyst for the oxygen reduction reaction†

Songlin Zhang, Yujiao Xie, Mengna Yang, Zhongying Li, Lulu Zhang, Jiahao Guo,* Jing Tang, Junming Chen and Xuchun Wang

The structural properties such as high specific surface area, good electrical conductivity, rich-defects of the catalyst surface guarantee outstanding catalytic performance and durability of oxygen reduction reaction (ORR) electrocatalysts. It is still a challenging task to construct ORR catalysts with excellent performance. Herein, we have reported column-like MoS_2/rGO with defect-rich ultrathin nanosheets prepared by a convenient solvothermal method. The structure and composition of MoS_2/rGO are systematically investigated. MoS_2/rGO shows a remarkable electrocatalytic performance, which is characterized by an outstanding onset potential of 0.97 V, a half-wave potential of 0.83 V, noticeable methanol tolerance, and durability of 93.7% current retention, superior to commercial Pt/C. The ORR process occurring on MoS_2/rGO is a typical four electron pathway. Therefore, this study achieves the design of a low-cost, highly efficient and stable nonprecious metal ORR electrocatalyst in alkaline media.

Received 7th May 2021
Accepted 30th June 2021

DOI: 10.1039/d1ra03552e

rsc.li/rsc-advances

1. Introduction

With the increasing depletion of fossil fuel resources as well as severely growing environmental problems, more and more attention has been paid to the development of new fuel cells (FCs) with high energy efficiency and extremely low emission of pollutants, which can sustainably produce electricity.[1–3] As the core reaction of FCs, the oxygen reduction reaction (ORR) in the cathode is more complicated and pivotal in obtaining better fuel cell performance.[4] Therefore, the ORR catalysts play a decisive role in the development and extensive commercialization of FCs.[5,6] Although they still possessed some fatal shortcomings, such as high costs, limited reserves, poor operational stability and easy poisoning, at present, Pt and its alloys are still the best ORR catalysts. These shortcomings have seriously restricted the commercialization development of FCs.[7,8] Therefore, fabricating high-performance, low-cost and perdurable ORR catalysts has become particularly urgent to promote the commercialization of fuel cells.

In the process of exploring alternatives to precious metal catalysts, scientists are paying more and more attention to transition metal compounds with a wide range of sources, environmental friendliness and easy synthesis. Recently, transition metal oxides,[9–14] carbides,[15–17] nitrides,[18–20] *etc.* have been gradually used as ORR catalysts, which have been proved to show good catalytic performance. The morphology, surface defects, and element vacancies of the catalyst were found to have extremely important influences on their electrocatalytic performance. Duan *et al.* have found large differences in the catalytic performance of Mn_3O_4 nanoparticles with different shapes integrated with nitrogen-doped graphene.[21] The improvement of the catalytic performance of the catalyst by oxygen vacancies (OVs) was demonstrated by Liu *et al.* They have argued that the improved catalytic activity is due to the fact that oxygen vacancies lower the band gap of oxide semiconductors, thereby improving their electrical conductivity, while oxygen vacancies provide a strong metal–support interaction.[22] The enriched oxygen vacancies on the MnO_x surface for the MONPMs/NC catalyst yielded a high ORR performance.[23] By controlling the Mo/S ratio in the synthesis process, Xie *et al.* achieved the control of the surface defects of MoS_2, and the catalytic performance of the defect-rich MoS_2 was obviously improved.[24] Among numerous transition metal compounds, inorganic graphene analogues (IGAs) with 2D ultrathin structures have attracted considerable attention because of their unique physical and chemical properties.[25,26] Because of the great differences between the inter- and intralayer bonds, these layered materials exhibit high anisotropy, which provides them an opportunity for practical applications. At present, IGAs are getting more and more applications in energy conversion devices.[27–30] As a typical IGA, the controllable synthesis and application of MoS_2 have been extensively studied. However, the research of ultrathin 2D MoS_2 as an ORR catalyst is still rare.

Herein, we report the preparation of a 3D column-like MoS_2/rGO catalyst stacked with ultrathin nanosheets by a solvothermal method. Such an interesting structure has accessible

College of Chemistry and Materials Engineering, Anhui Science and Technology University, Bengbu, Anhui, 233030, P. R. China. E-mail: guojiahao1974@163.com

† Electronic supplementary information (ESI) available: SEM, TEM and AFM of MoS_2, Raman spectrum of MoS_2/rGO, high-resolution XPS profiles of Mo 3d and S 2p of MoS_2, LSV and calculated K–L plots of MoS_2, rGO and Pt/C, the equivalent circuit model of EIS. See DOI: 10.1039/d1ra03552e

sites, maximized edges, and suitable interlayer distances to make it work as an effective ORR catalyst. As an intercalation agent for the exfoliation of 2D layered materials, 1-methyl-2-pyrrolidinone (NMP) can effectively prevent the aggregation of MoS_2 used as a solvent in the synthesis process, which plays a key role in the formation of this special structure. As a result, the 3D column-like MoS_2/rGO catalyst has revealed prominent ORR performance and durability with a typical four-electron path. The research opens new possibilities for controlling the morphology and structure of sulfides to optimize their ORR performance.

2. Experimental

2.1 Fabrication of ultrathin MoS_2/rGO

155 mg NaOH was ground into a powder and added quickly into 30 mL 1-methyl-2-pyrrolidinone (NMP, 99%) and 30 mg graphite oxide (GO), then 183 mg of sodium molybdate ($Na_2MoO_4 \cdot 2H_2O$, AR) and 363 mg L-cysteine [$HSCH_2CH(NH_2)COOH$, 98%] were added. After being stirred for 30 min, the solution was transferred to a Teflon-lined stainless steel autoclave with a capacity of 45 mL. The sealed vessel was then put into a 220 °C oven for 18 h and naturally cooled to room temperature. The black product was washed with anhydrous ethanol and deionized water successively three times and then dried at 80 °C under vacuum overnight. The sample was denoted as MoS_2/rGO. The synthesis procedure of MoS_2 is the same as that of MoS_2/rGO, except GO was not added.

2.2 Characterization techniques

The morphology of MoS_2/rGO and MoS_2 was studied by field emission scanning electron microscopy (FESEM, FEI HITACHI S-4800) and transmission electron microscopy (TEM, JEOJ-2010). The crystalline behavior of MoS_2/rGO and MoS_2 was analyzed by XRD (Rigaku D/max-rA) with Cu Kα radiation (λ = 0.154 nm, 2θ = 5–90°). The surface chemical compositions of MoS_2/rGO and MoS_2 were recorded on a Thermo ESCALAB 250 Xi with a Mg Kα (1253.6 eV) radiation exciting source. The sample surface area was determined with a Micromeritics ASAP 2460 system. Atomic force microscopy (AFM) was performed using a Veeco DI Nano-scope MultiMode V system. Raman spectra were recorded on a Senterra R200-L Raman microscope with a diode laser with excitation at 532 nm.

2.3 Electrochemical measurements

Electrochemical performance of the as-prepared catalysts was recorded on an electrochemical workstation (CHI 700E, Chenhua, Shanghai) using a conventional three-electrode system. The catalyst ink-coated rotating disk electrode (RDE, 5 mm in diameter) was used as a working electrode, a Pt wire as a counter electrode, a Ag/AgCl electrode as a reference electrode and 0.1 M KOH aqueous solution as the electrolyte. All the potentials in the experiment are converted to the relative hydrogen electrode (RHE) according to the formula $E_{RHE} = E_{Ag/AgCl} + 0.0592pH + E_{Ag/AgCl}^{\theta}$. Before each electrochemical experiment, the RDE was polished with Al_2O_3 (~0.1 μm) slurry and then cleaned with deionized water by ultrasonication to remove the residual Al_2O_3. 4 mg catalyst and 17 μL Nafion ionomer solution (5 wt%) were added into 1 mL ethanol and ultrasonically treated for 1 h to obtain a uniform catalyst ink. Subsequently, 5 μL of catalyst ink was dripped on the RDE surface and dried under ambient conditions to form the working electrode with a catalyst load of ~100 μg cm^{-2}. The same process is applied for the commercial Pt/C catalyst (20 wt%) as a comparison. After being passed with O_2/N_2 for 30 min, the electrolyte can be applied to electrochemical measurements and kept the ventilation state. The ORR catalytic activity of the catalyst was characterized by linear sweep voltammetry (LSV) and cyclic voltammetry (CV) within the potential window of 0–1.2 V (*vs.* RHE) by the RDE technique with a scan rate of 10 mV s^{-1}. The chronoamperometric method was used to evaluate the durability and methanol tolerance with 1600 rpm at 0.7 V (*vs.* RHE). To obtain the electron transfer number of per O_2, the rotation speed of the RDE varied from 400 to 2500 rpm. The electron transfer number is estimated through the following equations for slopes of Koutecky–Levich (K–L) plots obtained from LSV curves.[31]

$$\frac{1}{J} = \frac{1}{J_K} + \frac{1}{B\omega^{1/2}} \quad (1)$$

$$B = 0.2nF(D_O)^{2/3}\nu^{-1/6}c_O \quad (2)$$

where J and J_K signify the measured current density and the kinetic current density, ω denotes the rotating rate, and F stands for the Faraday constant (96 485 C mol^{-1}). D_O is the diffusion coefficient of O_2 in 0.1 M KOH (1.9×10^{-5} cm^2 s^{-1}). ν signifies the kinetic viscosity (0.01 cm^2 s^{-1}). c_O is the bulk concentration of O_2 (1.2×10^{-6} mol cm^{-3}). The constant 0.2 is applied when the unit of the rotation speed is in rpm.

3. Results and discussion

The morphology of the as prepared MoS_2/rGO sample was detected by SEM and TEM and is shown in Fig. 1. As can be seen from Fig. 1a, the MoS_2/rGO sample presents a column-like structure consisting of irregular MoS_2 nanosheets stacked

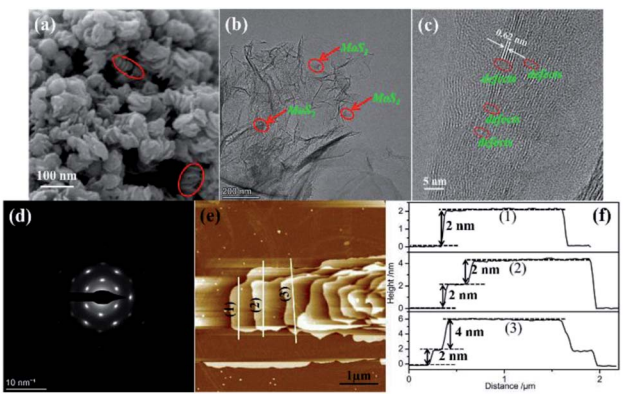

Fig. 1 (a) SEM image, (b) TEM image, (c) HRTEM image, (d) SEAD image, (e) AFM image and (f) height profiles from sections as indicated by the white lines of MoS_2/rGO.

together with each other. The diameter of the column-like structure is about 30–70 nm. Such an interesting 3D accessible nanostructure with the maximized edges and appropriate interlayer distance can be provided with more active sites for electrocatalytic reactions, which is beneficial to the improvement of catalytic activity. However, a nano-flowered structure formed by the hinges of the nanosheets of the resultant MoS_2 emerged when graphene was not added into the reaction system (Fig. S1†). The corresponding TEM image further authenticated that the MoS_2 nanosheets are grown on the surface of graphene for the MoS_2/rGO sample which shows a typical transparent film-like morphology as shown in Fig. 1b. A lattice fringe of 0.62 nm on the high-resolution transmission electron microscopy (HRTEM) images of MoS_2/rGO and MoS_2 samples is observed, as displayed in Fig. 1c, which belongs to the *d* spacing of the (002) lattice plane of MoS_2. Careful observation of the HRTEM images brings to light that rich defects and disordered structure emerged for the MoS_2/rGO sample, whereas MoS_2 did not. This phenomenon is attributed to the disorganization in the atomic arrangement caused by the addition of graphene during the formation of MoS_2. The existence of rich defects provides a large number of active sites of the MoS_2/rGO catalyst. The selected area electron diffraction (SEAD) pattern in Fig. 1d can be indexed to the pure phase for the adsorption and dissociation of O_2 on the catalyst surface, which is of great significance to the improvement of the catalytic hexagonal MoS_2 phase. The presence of clear diffraction spots revealed that the MoS_2 sheets of the MoS_2/rGO catalyst are composed of few layers. Atomic force microscopy (AFM) results were used to demonstrate the ultrathin structure of the synthesized MoS_2 materials. The AFM image of MoS_2/rGO (Fig. 1e) is confirmed once again; it has a column-like structure composed of nanosheets superimposed together. The AFM image and corresponding height profiles (Fig. 1e and f) showed that the average height of the MoS_2/rGO sheets is about 2 nm, which is significantly lower than the thickness of MoS_2 (Fig. S1e and S1f†). The ultrathin MoS_2 nanosheet partially retains the electron conjugation on the S–Mo–S layer, thus resulting in a better intrinsic conductivity than the polycrystalline MoS_2, which is beneficial to the improvement of its electrocatalytic activity.

To detect the crystalline structure of MoS_2/rGO and MoS_2 samples, X-ray powder diffraction patterns are measured and exhibited in Fig. 2a. For MoS_2 samples, the XRD pattern can be indexed to the hexagonal MoS_2 (JCPDS no. 37-1492). Four diffraction peaks at 17°, 32.2°, 33.7°, 39.3° and 57.1° can be assigned to the (002), (100), (101), (103) and (110) planes of the 2H-MoS_2, respectively. The diffraction peak position of the (002) plane is slightly higher than that of the standard card, suggesting subtle changes in its crystal structure. The XRD pattern of MoS_2/rGO is basically consistent with that of MoS_2. A new diffraction peak appears in the low-angle region, which corresponds to a (001) plane with a *d* spacing of 0.94 nm. This *d* spacing of 0.94 nm is larger than the 0.61 nm of the pristine 2H-MoS_2,[32,33] implying the appearance of a different layered structure in the samples, which may be due to the intercalation of NMP or the oxidized species of the initially MoS_2 nanosheets. Because NMP can be used as an intercalation agent for the

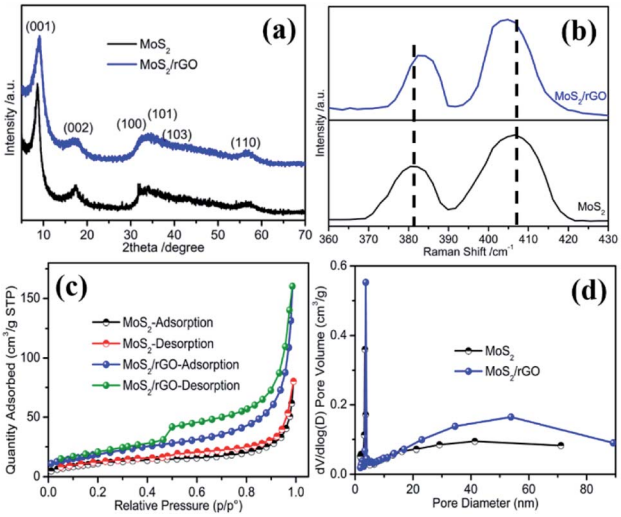

Fig. 2 (a) XRD patterns, (b) Raman spectrum, (c) nitrogen adsorption–desorption isotherms, and (d) the corresponding pore size distribution curves of MoS_2/rGO and MoS_2.

exfoliation of the two-dimensional layered materials, such as MoS_2, NMP can effectively prevent the aggregation of MoS_2 nanosheets and ultimately lead to the formation of (001) crystal planes with a larger *d* spacing during the reaction process when NMP is used as a solvent in the reaction system.[34,35] The asymmetrical shape of the (100) plane diffraction peaks indicates the stacking faults between the nanosheets, which may be due to the relative crystal plane sliding.[36]

Raman spectral analysis is an effective technique to detect the number of layers and defects of two-dimensional nanomaterials. As shown in Fig. S2,† the Raman spectrum of MoS_2/rGO exhibited two characteristic peaks located at 1352 and 1586 cm^{-1}, corresponding to the D band and G band of graphene, respectively, indicating the existence of graphene in the sample. The two MoS_2 samples also exhibited two characteristic peaks at low Raman shifts, as shown in Fig. 2b, which are the characteristic peaks of MoS_2. In general, MoS_2 has two Raman bands located at 380 and 408 cm^{-1}, corresponding to the E^1_{2g} and A_{1g} modes, respectively.[37] The former is caused by the in-plane vibration and the latter by the out-of-plane vibration of two sulfur atoms with the molybdenum atom within the S–Mo–S layer.[38] For MoS_2/rGO, two characteristic peaks are found at 382.3 and 404.8 cm^{-1}. It has been reported that the difference in Raman shifts between the two Raman peaks can be used to identify the number of layers of ultrathin MoS_2 crystals.[37] The difference value of 22.5 cm^{-1} for the MoS_2/rGO sample is obviously lower than the 26.3 cm^{-1} of MoS_2, suggesting the lower layer numbers of MoS_2/rGO. This observation is completely consistent with the AFM result, indicating that the as-prepared MoS_2/rGO sample has an ultrathin structure. The ultrathin structure is not only beneficial to the improvement of the electrical conductivity, but also to the increase of the active sites. Therefore, a better ORR performance can be predicted from the unique defect-rich MoS_2/rGO ultrathin nanosheets.

The surface area and porous structure of the two MoS_2 samples were characterized by nitrogen adsorption–desorption isotherm and pore size distribution analysis. It can be seen from Fig. 2c that the isotherms occupy an obvious hysteresis loop at a relative pressure of 0.45, which indicates a typical type IV adsorption, corresponding to a mesoporous structured material. The BET specific area of MoS_2/rGO is 71 $m^2\ g^{-1}$ with a pore volume of 0.165 $cm^3\ g^{-1}$, larger than those of MoS_2 (42 $m^2\ g^{-1}$ and 0.139 $cm^3\ g^{-1}$). The average pore size of MoS_2/rGO is 14 nm (Fig. 2d), which is also slightly larger than that of MoS_2 (8.6 nm). Larger pore sizes and porosity can provide rapid electrolyte transport and carrier-ion diffusion.

X-ray photoelectron spectroscopy (XPS) is an effective means to detect the chemical states of the elements on the catalyst surface. Fig. 3a displays the XPS characterization results of the samples. The MoS_2/rGO sample shows the characteristic peaks of Mo, S, C, and O, whereas the MoS_2 sample doesn't contain C element. The high-resolution XPS spectra of Mo 3d consisted of six peaks located at 226.6, 229.2, 230.0, 232.3, 233.2, and 236.3 eV, respectively (Fig. 3b). The small hump at 226.6 eV can be ascribed to sulfur 2s, which is in good agreement with previous reports.[39] For the as-prepared MoS_2/rGO, the two broad peaks centered at 232.5 and 229.3 eV can be resolved to two pair peaks, respectively. The former resolved peaks are located at 229.2 and 230.0, corresponding to Mo^{4+} d5/2 and the latter resolved peaks at 232.3 and 233.2 eV, corresponding to Mo^{4+} d3/2. The existence of the sixth XPS peak at 236.0 eV can be indexed to Mo^{6+} 3d5/2, which may be from the surface oxidation of MoS_2.[40] Compared with MoS_2 (Fig. S3a†), the peak of Mo^{6+} 3d5/2 for the MoS_2/rGO sample is extremely weak, indicating that MoS_2 is the main existence form of the MoS_2/rGO sample, which may be due to the reduction of graphene. It can be observed that the binding energy of Mo^{4+} of MoS_2/rGO samples is slightly negatively shifted compared to that of MoS_2, which may be the result of the interaction of Mo atoms with graphene. This interaction facilitates the electronic transfer between MoS_2 and graphene, resulting in the improvement of the catalytic performance of MoS_2/rGO. The S 2p XPS spectra of MoS_2 can be resolved into two sets of peaks that can be respectively assigned to S 2p3/2 located at 162.1 and 162.7 eV and S 2p3/2 located at 163.7 and 164.9 eV, respectively (Fig. S3b†). These two sets of peaks indicate that there are two forms of S: apical S^{2-} and bridging S_2^{2-} ligands, which explain the existence of a large number of Mo^{6+} on the surface of MoS_2.[41] In contrast, as shown in Fig. 3c, the S 2p spectra of MoS_2/rGO can only be decomposed into two peaks located at 162.4 and 163.7 eV, which is the characteristic peak of the S^{2-} in MoS_2. The deconvoluted C 1s spectrum consists of three peaks located at 284.9 eV, 285.7 and 289.1 eV, which could be assigned to the C–C, C–O, and COOH bonds, respectively (Fig. 3d). The total content of C–C and C–O bonds is 89%, indicating that GO was effectively reduced during the synthesis process, which is favorable for the firm recombination of MoS_2 and rGO. The value of S/Mo element ratio of MoS_2/rGO estimated from the integral peak area of the XPS spectra is ~2.0.

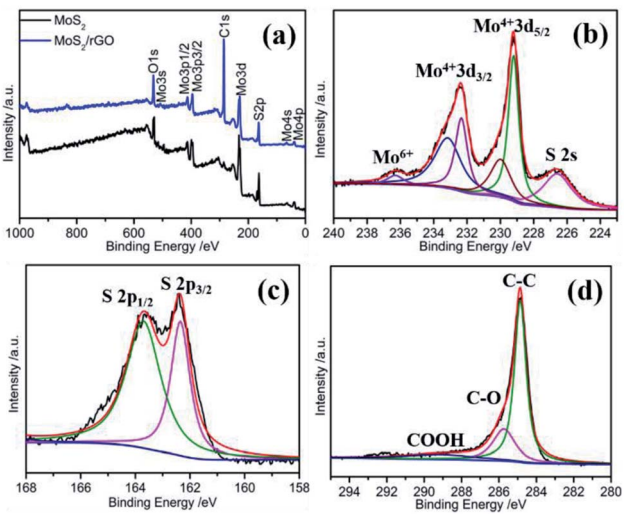

Fig. 3 (a) XPS spectrum. High-resolution XPS profiles of (b) Mo 3d, (c) S 2p and (d) C 1s of MoS_2/rGO.

Electrochemical methods were performed to verify the conjecture of the ORR electrocatalytic performance of the MoS_2/rGO catalyst. Fig. 4a portrays the cyclic voltammetry curves of various samples in 0.1 M KOH solution saturated with N_2 or O_2. The CV profiles of three samples in N_2-saturated 0.1 M KOH solution delivered no obvious reduction peaks. With the appearance of O_2 in 0.1 M KOH solution, the well-defined reduction peaks of O_2 located at 0.80 V for MoS_2/rGO, at 0.55 V for MoS_2, and at 0.78 V for rGO emerged and the current densities were 0.37, 0.24 and 0.27 mA cm^{-2}, respectively. The emergence of oxygen reduction peaks indicates the catalytic effect of the three samples for the ORR, in which the peak current and peak potential of MoS_2/rGO are significantly higher than those of rGO and MoS_2, suggesting its optimal catalytic performance.

To further investigate the ORR catalytic activity of MoS_2/rGO, these materials and commercial Pt/C were tested using a rotating disk electrode (RDE) in an O_2-saturated alkaline medium. The ORR polarization profiles of MoS_2, rGO, MoS_2/rGO, and Pt/C with a rotating rate of 1600 rpm are exhibited and compared in Fig. 4b. The onset (E_{onset}) and half-wave ($E_{1/2}$) potentials of rGO and MoS_2 were 0.88 V, 0.73 V and 0.68 V, 0.61 V, respectively, whereas the E_{onset} and $E_{1/2}$ of MoS_2/rGO significantly positively shifted to 0.98 V and 0.83 V, respectively. Both the E_{onset} and $E_{1/2}$ of MoS_2/rGO are very comparable to those of the Pt/C (E_{onset} = 0.99 V and $E_{1/2}$ = 0.85 V). Combined with the fact that its current density is close to the measured value of Pt/C, it is strongly recommended that MoS_2/rGO is a very effective ORR catalyst.

The LSV curves at the different rotating rates ranging from 400 to 2500 rpm were recorded to explore the reaction kinetics of the ORR catalyzed by MoS_2/rGO. Fig. 4d and S4† present a dramatic increase in the current density with an increasing rotating rate due to the reduced distance between the electrolyte and electrode. The K–L curves of different materials obtained by fitting according to the Koutecky–Levich equation at 0.4 V are shown in Fig. 4c. The fitting results all show a good linear relationship, indicating that the ORR is a first-order reaction.

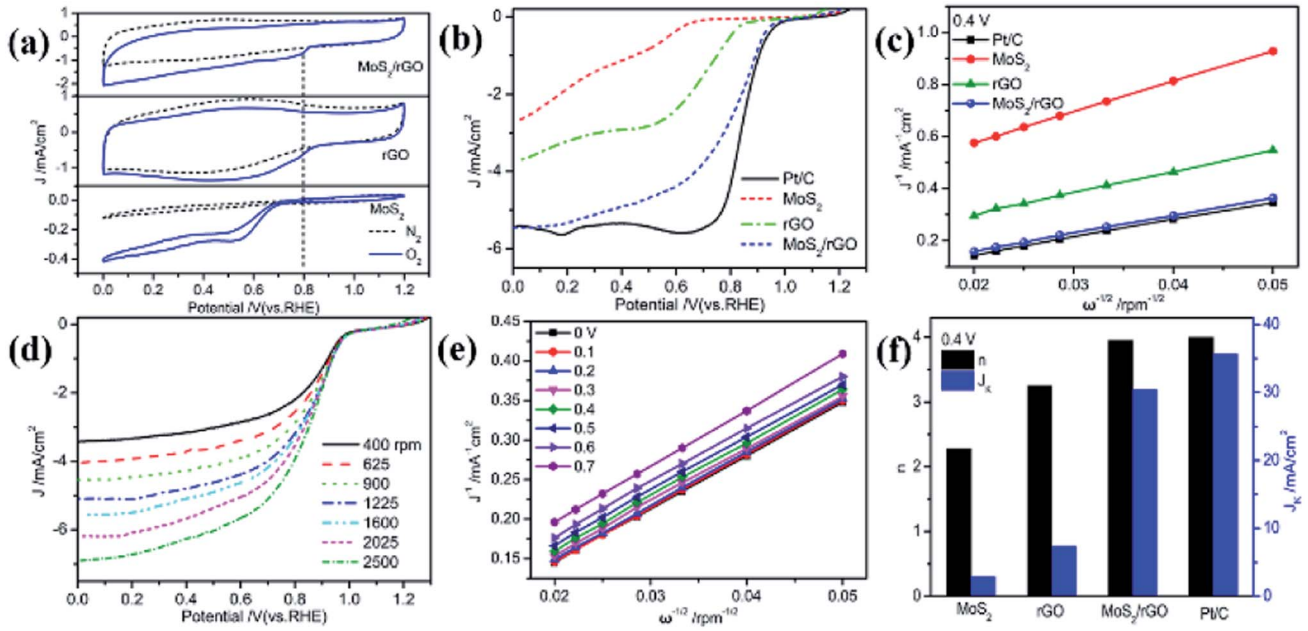

Fig. 4 (a) CV of three samples in N_2- and O_2-saturated 0.1 M KOH solution at a scan rate of 10 mV s^{-1}. (b) Linear sweep voltammetry (LSV) of three samples and Pt/C in O_2- saturated 0.1 M KOH at a scan rate of 10 mV s^{-1} with an RDE rotation rate of 1600 rpm. (c) K–L plots at 0.4 V of three samples and Pt/C. (d) LSV of MoS_2/rGO. (e) Calculated K–L plots of MoS_2/rGO. (f) Transferred electron number n and J_K of the ORR for three samples and Pt/C.

The K–L profile of MoS_2/rGO is closer to that of Pt/C than those of MoS_2 and rGO, and almost overlaps with that of Pt/C, indicating that MoS_2/rGO has almost the same catalytic performance as Pt/C. Fig. 4f displays the electron transfer number (n) and kinetic current (J_K) of the several samples and Pt/C for the ORR processes calculated from the slope and intercept of the K–L profiles at 0.4 V. The n value of MoS_2/rGO was found to be 3.95; in other words, the ORR process occurring on MoS_2/rGO is a four electron pathway, while that of MoS_2 is 2.28 and rGO is 3.25. The J_K value of MoS_2/rGO is 30.45 mA cm^{-2}, which is significantly higher than that of MoS_2 and rGO and closer to that of Pt/C (35.67 mA cm^{-2}). These electrochemical results have demonstrated the excellent catalytic performance of MoS_2/rGO for the ORR process, which is closely related to the special structure of the ultrathin stacked nanosheets.

From the comparison of MoS_2 and MoS_2/rGO, it is found that GO has an important influence on the morphology, surface defects and catalytic activity of MoS_2/rGO, so it is necessary to conduct a systematic research on the influence of GO content on the catalytic activity of MoS_2/rGO during the synthesis procedure. The results of the effect on the catalytic activity of MoS_2/rGO with different GO contents added in the synthesis procedure are shown in Fig. S5.† The result shows that the E_{onset} of MoS_2/rGO gradually increases with the increase of GO content, reaching the maximum when the GO content is 30 mg, and subsequently decreases. The change trend of current is the same. The results of n value and J_K also indicate the optimal catalytic activity of MoS_2/rGO with 30 mg of the GO content. It can be seen that GO plays an important role in the formation of MoS_2/rGO. The presence of GO disrupts the MoS_2 structure, leading to the production of numerous surface defects.

Tafel polarization profiles were used to confirm the ORR catalytic activity of MoS_2/rGO. As shown in Fig. 5a, the Tafel slope of MoS_2/rGO is −53 mV dec^{-1}, which is very close to the −40 mV dec^{-1} of Pt/C and far below the −206 mV dec^{-1} of MoS_2 and −103 mV dec^{-1} of rGO. Such results again suggest the excellent ORR catalytic performance of MoS_2/rGO. The electrical conductivity of the catalytic material has an important effect on

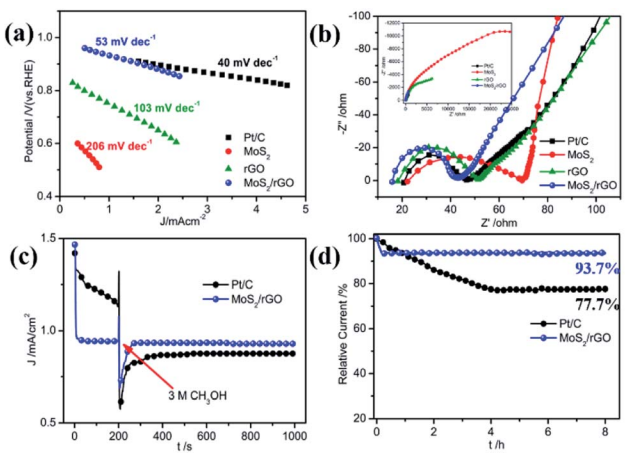

Fig. 5 (a) Tafel plots of the three samples and Pt/C. (b) EIS of the three samples and Pt/C. (c) i–t chronoamperometric response of MoS_2/rGO and Pt/C with the addition of 3 M methanol. (d) Chronoamperometric response of MoS_2/rGO and Pt/C. Tests were conducted in O_2-saturated 0.1 M KOH solution at 0.7 V.

the electron transfer of the catalytic reaction, thus affecting its catalytic performance. Electrochemical impedance spectroscopy (EIS) experiments were performed to characterize the electron transfer process of the ORR process on MoS_2/rGO. The EIS Nyquist plots of the three samples and commercial Pt/C are shown in Fig. 5b and the resultant EIS data are obtained from the equivalent circuit model shown in Fig. S6.† The high frequency intercept on the real axis determines the serial resistance (R_s), which is usually caused by bulk resistance, conductivity of the catalyst and adhesion between the catalyst and GC substrate. The R_s values of MoS_2/rGO, rGO, MoS_2 and Pt/C are 15.88, 18.19, 22.16 and 20.63 Ω, respectively. MoS_2/rGO occupies the lowest R_s, indicating its best electrical conductivity, which is caused by its graphene analogue properties and ultrathin structure. The high frequency region possesses a semicircle, which is caused by the electron transfer resistance during the oxygen reduction reaction. The diameter value reflects the electrocatalytic activity of the catalytic material for the ORR. R_{ct} increases in the order of Pt/C (25.96 Ω) < MoS_2/rGO (27.21 Ω) < rGO (33.20 Ω) < MoS_2 (47.29 Ω), indicating the best electrocatalytic activities of MoS_2/rGO for the ORR in the three catalysts, even close to Pt/C. This is in full agreement with previous characterization results.

The methanol tolerance and durability of the ORR catalyst are two important performance parameters for their practical application in fuel cells. During the operation of the direct methanol fuel cell (DMFC), the methanol can penetrate to the cathode through the proton exchange membrane and react on the cathode catalyst to poison the ORR catalyst by methanol oxidation and result in the deactivation of ORR activities, which seriously affects the performance of the fuel cell. Consequently, a desirable ORR catalyst should have favorable selectivity, and its reaction to methanol oxidation during the ORR catalytic process should be inert. Chronoamperometric analysis at 0.7 V was used to examine the methanol tolerance of the MoS_2/rGO catalyst toward ORR activity to explore the practical application of an active electrocatalyst in fuel cells, as presented in Fig. 5c. Prior to the addition of 3 M methanol into the KOH electrolyte, the commercial Pt/C catalyst showed significantly higher current density than MoS_2/rGO which slowly decreased, indicating good but unstable catalytic activity of Pt/C. With the addition of methanol, the current of the Pt/C catalyst rapidly decreased to a lower value and gradually stabilized. The current decrease is due to the competitive reaction of the ORR with methanol oxidation on the catalyst's surface resulting from the inferior selectivity and sensitivity of the commercial Pt/C catalyst. For the MoS_2/rGO catalyst, a significant change of the current density did not emerge after the presence of methanol under the same experimental conditions. These facts fully demonstrate the outstanding methanol tolerance and superhigh ORR selectivity of the MoS_2/rGO catalyst. Long-term durability is another important property of an excellent ORR catalyst in practical application of fuel cells and can also be measured by chronoamperometric analysis. Fig. 5d shows the chronoamperometric profiles of MoS_2/rGO and Pt/C catalysts at a potential of 0.7 V in O_2-saturated 0.1 M KOH. The durability comparison showed that after 8 hours of operation, 93.7% of the initial current still remains for the MoS_2/rGO catalyst, whereas the residual current of Pt/C only retains 77.7% of the initial current. The results showed that the MoS_2/RGO catalyst demonstrates a much more outstanding durability than Pt/C.

The results of electrochemical experiments verify our prediction of the ORR catalytic activity of the MoS_2/RGO catalyst. The particularity of the morphology and structure guarantees excellent ORR catalytic activity of MoS_2/rGO. The column-like structure stacked by the ultrathin nanosheets of MoS_2 provides a large surface area and mesoporous structure for the catalyst material which provide a rapid electron/ion transport path and abundant channel for the transport of the electrolyte and reactant particles in the ORR process. The ultrathin nanosheets and the interaction of Mo atoms with graphene enhance the electrical conductivity of the composite material which can ensure the fast electron transfer and low charge transfer resistance. The rich-defects of the nanosheets provide sufficient active sites for the adsorption and dissociation of O_2. It is the particularity of these structures that ensures its outstanding ORR catalytic performance.

4. Conclusions

In summary, column-like MoS_2/rGO with defect-rich ultrathin nanosheets was prepared by a convenient solvothermal method as the ORR catalyst for fuel cell applications. The MoS_2/rGO composite catalyst has an ultrathin layered structure, rich defects, large surface area, mesoporous structure, and interaction between MoS_2 and graphene. As the ORR catalyst, the MoS_2/rGO composite catalyst showed an excellent ORR performance, which is characterized by the higher onset potential, half-wave potential and current density. The transferred-electron number of the ORR process is 3.95, which means that the ORR process occurring on the MoS_2/rGO composite catalyst is a typical four electron pathway. Meanwhile, the MoS_2/rGO composite catalyst also exhibits outstanding methanol tolerance and long-term durability. Hence, this investigation has provided an inexpensive, efficient, and stable cathode catalyst used as a substitute for Pt to probe the feasibility of promoting the commercialization of fuel cells.

Conflicts of interest

There are no conflicts to declare.

Acknowledgements

We thank the Natural Science Foundation of Anhui Province (1808085MB31), Students Platform for Innovation and Entrepreneurship Training Program of China (S201910879298), Stable Talent Foundation of Anhui Science and Technology University (HCWD201601), National Natural Science Foundation of China (21904004), and Science and Technology Major Project of Anhui Province (18030901087) for their financial support.

Notes and references

1 D. Guo, R. Shibuya, C. Akiba, S. Saji, T. Kondo and J. Nakamura, *Science*, 2016, **351**, 361.
2 S. K. Singh, K. Takeyasu and J. Nakamura, *Adv. Mater.*, 2019, **31**, 1804297.
3 Y. J. Wang, W. Long, L. Wang, R. Yuan, A. Ignaszak, B. Fang and D. P. Wilkinson, *Energy Environ. Sci.*, 2018, **11**, 258.
4 C. Chen, Y. Kang, Z. Huo, Z. Zhu, W. Huang, H. L. Xin, J. D. Snyder, D. Li, J. A. Herron, M. Mavrikakis, M. Chi, K. L. More, Y. Li, N. M. Markovic, G. A. Somorjai, P. Yang and V. R. Stamenkovic, *Science*, 2014, **343**, 1339.
5 Z. P. Cano, D. Banham, S. Ye, A. Hintennach, J. Lu, M. Fowler and Z. Chen, *Nat. Energy*, 2018, **3**, 279.
6 P. Zhang, F. Sun, Z. H. Xiang, Z. G. Shen, J. Yun and D. P. Cao, *Energy Environ. Sci.*, 2014, **7**, 442.
7 D. Zeng, X. Yu, Y. Zhan, L. Cao, X. Wu, B. Zhang, J. Huang, Z. Lin, F. Xie, W. Zhang, J. Chen, W. Xie, W. Mai and H. Meng, *Int. J. Hydrogen Energy*, 2016, **41**, 8563.
8 S. K. Singh, V. Kashyap, N. Manna, S. N. Bhange, R. Soni, R. Boukherroub, S. Szunerits and S. Kurungot, *ACS Catal.*, 2017, **7**, 6700.
9 W. Zhao, X. Li, R. Yin, L. Qian, X. Huang, H. Liu, J. Zhang, J. Wang, T. Ding and Z. Guo, *Nanoscale*, 2019, **11**, 50.
10 Y. Sun, Z. Liu, W. Zhang, X. Chu, Y. Cong, K. Huang and S. Feng, *Small*, 2019, **15**, 1803513.
11 W. Xia, R. Zou, L. An, D. Xia and S. Guo, *Energy Environ. Sci.*, 2015, **8**, 568.
12 T. N. Lambert, J. A. Vigil, S. E. White, C. J. Delker, D. J. Davis, M. Kelly, M. T. Brumbach, M. A. Rodriguez and B. S. Swartzentruber, *J. Phys. Chem. C*, 2017, **121**, 2789.
13 L. Zhang, X. Yang, R. Cai, C. Chen, Y. Xia, H. Zhang, D. Yang and X. Yao, *Nanoscale*, 2019, **11**, 826.
14 Y. Yang, Y. Wang, Y. Xiong, X. Huang, L. Shen, R. Huang, H. Wang, J. P. Pastore, S.-H. Yu, L. Xiao, J. D. Brock, L. Zhuang and H. D. Abruña, *J. Am. Chem. Soc.*, 2019, **141**, 1463.
15 L. Song, T. Wang, L. Li, C. Wu and J. He, *Appl. Catal., B*, 2019, **244**, 197.
16 G. Ren, X. Lu, Y. Li, Y. Zhu, L. Dai and L. Jiang, *ACS Appl. Mater. Interfaces*, 2016, **8**, 4118.
17 M. Xiao, J. Zhu, L. Feng, C. Liu and W. Xing, *Adv. Mater.*, 2015, **27**, 2521.
18 X. Tian, J. Luo, H. Nan, H. Zou, R. Chen, T. Shu, X. Li, Y. Li, H. Song, S. Liao and R. R. Adzic, *J. Am. Chem. Soc.*, 2016, **138**, 1575.
19 M. E. Kreider, A. Gallo, S. Back, Y. Liu, S. Siahrostami, D. Nordlund, R. Sinclair, J. K. Nørskov, L. A. King and T. F. Jaramillo, *ACS Appl. Mater. Interfaces*, 2019, **11**, 26863.
20 X. Huang, Z. Yang, B. Dong, Y. Wang, T. Tang and Y. Hou, *Nanoscale*, 2017, **9**, 8102.
21 J. Duan, S. Chen, S. Dai and S. Z. Qiao, *Adv. Funct. Mater.*, 2014, **24**, 2072.
22 G. Liu, J. Li, J. Fu, G. Jiang, G. Lui, D. Luo, Y.-P. Deng, J. Zhang, Z. P. Cano, A. Yu, D. Su, Z. Bai, L. Yang and Z. Chen, *Adv. Mater.*, 2018, **31**, 1806761.
23 Y. Zhang, C. Wang, J. Fu, H. Zhao, F. Tian and R. Zhang, *Chem. Commun.*, 2018, **54**, 9639.
24 J. Xie, H. Zhang, S. Li, R. Wang, X. Sun, M. Zhou, J. Zhou, X. W. (David) Lou and Y. Xie, *Adv. Mater.*, 2013, **25**, 5807.
25 J. Feng, X. Sun, C. Wu, L. Peng, C. Lin, S. Hu, J. Yang and Y. Xie, *J. Am. Chem. Soc.*, 2011, **133**, 17832.
26 K. S. Kim, Y. Zhao, H. Jang, S. Y. Lee, J. M. Kim, K. S. Kim, J. H. Ahn, P. Kim, J. Y. Choi and B. H. Hong, *Nature*, 2009, **457**, 706.
27 K. Krishnamoorthy, P. Pazhamalai, G. K. Veerasubramani and S. J. Kim, *J. Power Sources*, 2016, **321**, 112.
28 J. Guo, Y. Shi, X. Bai, X. Wang and T. Ma, *J. Mater. Chem. A*, 2015, **3**, 24397.
29 Y. Zhang, Y. Li, H. Li, F. Yin, Y. Zhao and Z. Bakenov, *J. Nanopart. Res.*, 2016, **18**, 63.
30 G. Ye, Y. Gong, J. Lin, B. Li, Y. He, S. T. Pantelides, W. Zhou, R. Vajtai and P. M. Ajaya, *Nano Lett.*, 2016, **16**, 1097.
31 Y. Wang, N. Guo, L. Zhu, Y. Pan, R. Wang, Z. Zhang and S. Qiu, *Chem. Commun.*, 2018, **54**, 12974.
32 M.-R. Gao, M. K. Chan and Y. Sun, *Nat. Commun.*, 2015, **6**, 7493.
33 J. Xie, J. Zhang, S. Li, F. Grote, X. Zhang, H. Zhang, R. Wang, Y. Lei, B. Pan and Y. Xie, *J. Am. Chem. Soc.*, 2013, **135**, 17881.
34 J. R. Brent, D. J. Lewis, T. Lorenz, E. A. Lewis, N. Savjani, S. J. Haigh, G. Seifert, B. Derby and P. O'Brien, *J. Am. Chem. Soc.*, 2015, **137**, 12689.
35 E. P. Nguyen, B. J. Carey, T. Daeneke, J. Z. Ou, K. Latham, S. Zhuiykov and K. Kalantar-Zadeh, *Chem. Mater.*, 2015, **27**, 53.
36 J. Ding, Y. Zhou, Y. Li, S. Guo and X. Huang, *Chem. Mater.*, 2016, **28**, 2074.
37 H. Li, Q. Zhang, C. Chong, R. Yap, B. K. Tay, T. H. T. Edwin, A. Olivier and D. Baillargeat, *Adv. Funct. Mater.*, 2012, **22**, 1385.
38 S. Tongay, H. Sahin, C. Ko, A. Luce, W. Fan, K. Liu, J. Zhou, Y.-S. Huang, C.-H. Ho, J. Yan, D. F. Ogletree, S. Aloni, J. Ji, S. Li, J. Li, F. M. Peeters and J. Wu, *Nat. Commun.*, 2014, **5**, 3252.
39 C. J. Liu, S. Y. Tai, S. W. Chou, Y. C. Yu, K. D. Chang, S. Wang, F. S. S. Chien, J. Y. Lin and T. W. Lin, *J. Mater. Chem.*, 2012, **22**, 21057.
40 Y. M. Sun, X. L. Hu, W. Luo and Y. H. Huang, *ACS Nano*, 2011, **5**, 7100–7107.
41 J. Kibsgaard, Z. Chen, B. N. Reinecke and T. F. Jaramillo, *Nat. Mater.*, 2012, **11**, 963.